



Lacunarity exponent and Moran index: A complementary methodology to analyze AFM images and its application to chitosan films

Erveton P. Pinto ^{a,*}, Marcelo A. Pires ^b, Robert S. Matos ^{a,c}, Robert R.M. Zamora ^a, Rodrigo P. Menezes ^d, Raquel S. Araújo ^{a,e}, Tiago M. de Souza ^f

^a Universidade Federal do Amapá, Amapá 68903-419, Brazil

^b Centro Brasileiro de Pesquisas Físicas, Rio de Janeiro 22290-180, Brazil

^c Universidade Federal de Sergipe, Sergipe 49100-000, Brazil

^d Pontifícia Universidade Católica do Rio de Janeiro, Rio de Janeiro 22541-041, Brazil

^e Universidade Federal de Ouro Preto, Minas Gerais 35400-000, Brazil¹

^f Universidade do Estado do Amapá, Amapá 68900-070, Brazil

ARTICLE INFO

Article history:

Received 24 April 2021

Received in revised form 28 May 2021

Available online 18 June 2021

Keywords:

Fractal lacunarity

Spatial autocorrelation

Surface topography

Polymeric films

Glycerol

ABSTRACT

In this work, we developed new scripts to calculate the lacunarity exponent and Moran's index of Atomic Force Microscopy (AFM) images. The lacunarity exponent was estimated by combining the Otsu binarization and gliding-box algorithm, and Moran index was introduced to evaluate the surfaces' spatial autocorrelation. Developed scripts were first validated using numerical simulation of self-similar fractal and self-affine isotropic surfaces. Then, we successfully synthesized chitosan films with different glycerol concentrations and used the lacunarity and Moran's index for a thorough characterization. The validation of the proposed scripts using simulated Sierpinski Carpets and 3D artificial surfaces showed promising potential for analyzing AFM images. Finally, the methodology application to AFM images of chitosan films suggested that lacunarity analysis and Moran index determination could complement thin films' quality processing control.

© 2021 Published by Elsevier B.V.

1. Introduction

Atomic Force Microscopy (AFM) is one of the most advanced and powerful techniques for scanning, measuring, and analyzing surfaces. Its high resolution reaches the atomic level, allowing the evaluation of particles' spatial distribution on surfaces, a factor that influences several interface phenomena, such as wear, friction, and adhesion [1–3]. It allows the obtention of tridimensional images of solid surfaces in contact with air, liquid, and others with minimum sample preparation [4,5].

The processing of AFM images has been widely studied to obtain surface parameters [6–13]. The texture of real surfaces usually shows self-affinity at some scales, which allows the modeling of its structure as a self-affine fractal. Unlike self-similar fractal that is isotropic and scale-invariant, the similarity of self-affine ones is only statistical [14]. The statistical patterns are closely related to the image's pixel distribution, corresponding to the AFM surface's heights. The fractal dimension reflects how denser the set of pixels is and provides a statistical index of complexity, which indicates how pattern details change with the scale. The higher the fractal dimension, the stronger the pattern's persistence [7,14–17].

* Corresponding author.

E-mail address: erveton@unifap.br (E.P. Pinto).

¹ Present address.

Different objects can present the same fractal dimension and utterly different texture patterns [8,14,18–20]. Mandelbrot [18] introduced the lacunarity measurement to differentiate such objects, which later proved to be effective for non-fractal ones [19,20]. Lacunarity describes, at various scales, the distribution of lacunas (void spaces) within a data set (like the height matrix of an AFM image). High lacunarity exponent values indicate a heterogeneous arrangement of lacunas, whereas low one's depict a tendency to a homogeneous distribution [8,18–20].

In the microscopy field, fractals present significant contributions about magnification's and scale's effects on morphology, providing critical concepts for understanding and quantifying some aspects of randomness, irregularity, complexity, shapes and patterns self-similarity [20]. Nonetheless, only the fractal dimension is given by commercial image processing programs [8]. There is still no consensus about the best methodology to determine fractal lacunarity, and different algorithms have already been proposed for this purpose [8,20–24].

Dias et al. [22] used ImageJ software and Fraclac plugin, adapted with the differential box-counting algorithm, to determine lacunarity and identify stains patterns in 8-bits-grayscale images of rough metal surfaces. The authors concluded that lacunarity measurements are suitable to monitor defects or roughness variations of metal surfaces. The same software and plugin were applied by Pander et al. [24] for the analysis of carbon nanotube forestry-like catalysts surfaces using AFM images converted into grayscale. The comparison of fractal analysis and Raman mapping distributions revealed different catalyst's annealing stages.

Binary and grayscale methods were also used for computing lacunarity and their accuracy to classify urban features remotely detected [21]. The authors used the gliding-box and differential box-counting algorithms to estimate lacunarity of binary and grayscale images, respectively. Their results highlighted the spectrum-based classification inaccuracy (55%) compared to lacunarity approach (92%). The differential box-counting algorithm was also used by Țălu et al. [8] for the lacunarity analysis of AFM images from silver/diamond-like carbon nanocomposite film. Fractal lacunarity showed to be useful in advanced surface image characterization.

Fraclac plugin of ImageJ software is generally used to determine the fractal lacunarity of digital images, but it only allows evaluating 8-bits grayscale images or in RGB format. Although helpful, it is too limited to analyze AFM data. Works based on algorithms written in C++ [21] and Fortran [8] languages undoubtedly represent an advance. Therefore, the fractal lacunarity potential for analysis of AFM images remains unexplored and deserves deeper investigations to establish an efficient and accurate evaluation methodology.

Another parameter that seems interesting to analyze AFM images is the Moran Index. It is the most widespread spatial analysis tool for characterizing area units' spatial autocorrelation [25–31]. Such parameter is a standardized measure of the correlation between observations in neighboring areas and is commonly used to analyze geographic data. Cocu et al. [25] used Moran's index to investigate spatial autocorrelation of annual abundance for the pest aphid *Myzus persicae* collected in suction traps distributed across north-west Europe. The authors concluded that trap data could provide representative information for large geographical areas and can be used to estimate the species' aerial abundance. Moran index was also used by Shirzadi et al. [31] to determine the spatial distribution of cutaneous leishmaniasis in northeastern Iran. Spatial analysis indicated that the disease incidence presented a cluster pattern, showing high-risk areas, which can be used in controlling and prevention tools.

Considering these aspects, we developed algorithms in the R language [32] to calculate the fractal lacunarity and Moran index of AFM topography images using the measured height matrix. Scripts validation was carried out by numerical simulation of self-similar fractal and 3D artificial surfaces with controlled roughness. Afterward, algorithms were applied to analyze the fractal lacunarity and Moran Index of chitosan films, a promising material for the biomedical field [33–39].

2. Materials and methods

2.1. Fractal dimension

Fractal dimension (D_f) values were calculated using Gwyddion software [40]. We used the box-counting algorithm to determine the minimum number of squares $[N(s)]$ of side s needed to cover the entire set. According to Mandelbrot [14], $N(s)$ obeys a power law of type $N(s) = \gamma \cdot s_f^{-D}$, where D_f is the fractal dimension and γ is an arbitrary constant. Therefore, D_f was determined by the slope of the $\text{Log}[N(s)]$ versus $\text{Log}[1/s]$ curve.

2.2. Fractal lacunarity

Lacunarity is a complementary measure of the fractal dimension that allows a better description of their texture. We proposed a new method for calculating lacunarity of AFM images based on the combination of the gliding-box algorithm [21,23,41–43] with the Otsu binarization [44–46], which was written in R language.

For binarization, a height value k was used to separate the heights (varying from 0 to h) into C_0 and C_1 classes. C_0 and C_1 indicate pixels with heights varying in the $[0, \dots, k-1]$ and $[k, \dots, h]$ ranges. The occurrence probabilities of C_0 and C_1 were given by $W_0 = n_0/N$ and $W_1 = n_1/N$, respectively (where n_0 and n_1 are the number of times each class occurs and N is the total number of pixels). Mean heights of the respective classes (μ_0 and μ_1) were calculated using Eqs. (1) and (2).

$$\mu_0 = \sum_{i=0}^{k-1} i \cdot \frac{n_i}{n_0}, \quad (1)$$

$$\mu_1 = \sum_{i=k}^h i \cdot \frac{n_i}{n_1}, \quad (2)$$

For each height i , conditions (3) and (4) must be fulfilled:

$$W_0 \cdot \mu_0 + W_1 \cdot \mu_1 = \mu_T, \quad (3)$$

$$W_0 + W_1 = 1, \quad (4)$$

where μ_T is the average of the matrix's height values.

The variances of C_0 and C_1 were given by Eqs. (5) and (6).

$$\sigma_0^2 = \sum_{i=0}^{k-1} (i - \mu_0)^2 \cdot \frac{n_i}{n_0}, \quad (5)$$

$$\sigma_1^2 = \sum_{i=k}^h (i - \mu_1)^2 \cdot \frac{n_i}{n_1}, \quad (6)$$

The class variance and the variance between classes were calculated using Eqs. (7) and (8), respectively [44].

$$\sigma_W^2 = W_0 \cdot \sigma_0^2 + W_1 \cdot \sigma_1^2, \quad (7)$$

$$\sigma_B^2 = W_0 \cdot (\mu_0 - \mu_T)^2 + W_1 \cdot (\mu_1 - \mu_T)^2 = W_0 \cdot W_1 \cdot (\mu_0 - \mu_1)^2, \quad (8)$$

To evaluate the efficiency of the threshold at height k , we used a measure of class separability, Eq. (9) [47]. According to this criterion, the best threshold k^* is the one that maximizes the separability, as shown in Eq. (10).

$$\eta = \frac{\sigma_B^2}{\sigma_T^2}, \quad (9)$$

$$k^* = \operatorname{argmax}[\eta], \quad (10)$$

where $\sigma_T^2 = \sigma_W^2 + \sigma_B^2$ is the variance of the matrix's height values.

The maximum value of $\eta(k^*)$ can be used as a class separability measure of the original image or histogram bimodality. This parameter is invariant under similar scale transformations and varies within the range:

$$0 \leq \eta(k^*) \leq 1, \quad (11)$$

where the lower (zero) and upper (one) limits correspond to images presenting single and double heights values, respectively.

After calculating the optimal threshold (k^*), AFM images were binarized following the condition represented by Eq. (12). Each height was represented by a function $z(x, y)$, where x and y correspond to the pixel's coordinates.

$$g(x, y) = \begin{cases} 1 & \text{if } z(x, y) \geq k^* \\ 0 & \text{otherwise} \end{cases}. \quad (12)$$

The gliding-box algorithm was used to evaluate the distribution of lacunar pixels in the binary images. A square box of length r slides over the image from the upper right corner to the bottom left one, advancing a column and a line per scan, whereas the number of lacunar pixels p inside the box is counted (Fig. 1).

The number of r -length boxes with p lacunar pixels is given by the frequency distribution $n(p, r)$, whereas the probability distribution $Q(p, r)$ is calculated using Eq. (13). Here, each position occupied by the box is considered a new box.

$$Q(p, r) = \frac{n(p, r)}{N(r)}, \quad (13)$$

where $N(r) = (\Delta_a - r + 1) \cdot (\Delta_b - r + 1)$ is the total number of possible boxes for a given value of r , and Δ_a and Δ_b is the number of pixels corresponding to the image's height and base, respectively. Thus, according to the literature [18], the lacunarity $L(p, r)$ can be calculated using Eq. (14).

$$L(p, r) = \frac{\sum p^2 \cdot Q(p, r)}{[\sum p \cdot Q(p, r)]^2}, \quad (14)$$

The lacunarity drop with the r increasing can be expressed by a power law of type $L(p, r) = \alpha \cdot r^{-\beta}$, where β is the exponent of lacunarity and α is an arbitrary constant. Thus, the exponent of lacunarity (β) can be determined by the slope of the $\ln[L(p, r)]$ versus $\ln[r]$ curve, Eq. (15).

$$\ln[L(p, r)] = \ln[\alpha] + \beta \ln[r], \quad (15)$$

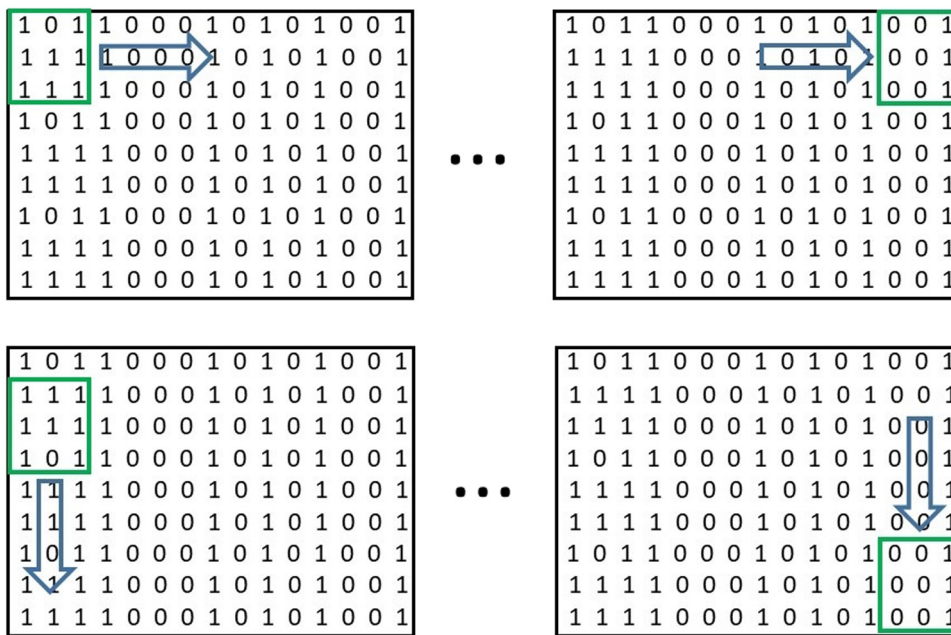


Fig. 1. Illustration of the gliding-box algorithm for a square box with length $r = 3$ running on a 15×9 pixel binary image.

When r tends to r_{\max} (for example, $r_{\max} = 256$ for a 256×256 pixels image), the lacunarity value and lacunarity exponent tend to 1 and zero, respectively. β is invariant to scale transformations [48], revealing how lacunar patterns persist in different parts of the image. The closer β is to zero, the more homogeneous the surface becomes. Scripts developed to calculate the Otsu threshold and the fractal lacunarity were presented in Appendix A.

2.3. Moran's index

According to the literature [25–31], Moran Index (I) is a standardized measure of spatial autocorrelation among variables of neighboring areas, varying in the range of -1 to 1 . For height data obtained from AFM images, an index $I = 0$ reveals spatial independence of heights distribution throughout the surface (perfect randomness). A positive index ($I > 0$) indicates the grouping degree of similar heights and a perfect clustering when $I = 1$. In contrast, a negative index ($I < 0$) demonstrates the grouping degree of different heights and represents an ideal dispersion when $I = -1$.

The spatial autocorrelation analysis was conducted using the queen contiguity neighborhood [49]. From the neighborhood criterion, pairs of areas i and j were represented by the spacial weight $W_{ij} = 1$ and $W_{ij} = 0$ when they were connected or not, respectively. Moran index was calculated according to Eq. (16).

$$I = \frac{N}{\sum_i \sum_j W_{ij}} \frac{\sum_i \sum_j W_{ij} (Z_i - \mu) (Z_j - \mu)}{\sum_i (Z_i - \mu)^2}, \tag{16}$$

where N is the total number of areas, Z_i and Z_j are the height values of areas i and j , respectively, and μ is the height average of areas i and j .

A script was developed to generate a Moran correlogram (Appendix A), which is a graph of the Moran index against distance lags (1st, 2nd, ..., n th neighborhood) [25]. The correlograms were generated using the *sp.correlogram* function from *spdep* package [50] written in R language.

2.4. Validation of R-scripts developed to calculate fractal lacunarity and Moran index

The R-script for lacunar analysis was first applied to the Sierpinski Carpet fractal [51]. This fractal ($D_f \sim 2.79$) was built by dividing a square into nine parts, from which the central one was removed. This procedure was repeated recursively to the eight remaining subsquares to generate fractal images of 81×81 , 243×243 , and 729×729 pixels using an adapted script openly available [52].

Before analyzing real images, R-scripts for calculation of Moran Index and fractal lacunarity were validated using artificial surfaces with controlled roughness parameters. Self-affine rough surfaces with power spectral density (PSD) given by a power-law and fractal's spectrum region depending on Hurst exponent (H) were simulated according to Persson et al. [53]. We employed the rough surface package from Ref. [54]. The artificial height-matrix was generated

Table 1
Formulations of chitosan films.

Formulation	Chitosan (% m/v de solution)	Glycerol (% m/m of chitosan)
#1	2	0
#2	2	3
#3	2	25

using Fourier transform and the Monte Carlo method [55,56]. Artificial surfaces with different Hurst exponents (0.10, 0.30, 0.50, 0.70, and 0.90) were simulated in triplicate (Appendix B). The height matrices were extracted to generate 3D images of 256×256 pixels.

2.5. Synthesis of chitosan films

Chitosan films were prepared using the casting method [38,39]. Chitosan powder (low molecular weight and deacetylation of 95%) (Sigma-Aldrich®, Brazil) and glycerol (Alphatec Química Fina®, Brazil) were dissolved in glacial acetic acid (3% v/v) (Cromaline Química Fina Ltda®, Brazil) to obtain a film-forming solution with 2% (m/v) of polymer and different concentrations of glycerol, as shown in Table 1. The film-forming solution was stirred at room temperature ($25 \pm 2^\circ\text{C}$) for 2 h, and their aliquots (40 ml) deposited in glass Petri dishes (90 mm in diameter) for drying at room temperature during 5 days. After detachment from the dishes, the samples were individually stored in a sterile bag until analysis.

2.6. AFM images

Topographic images were obtained using atomic force microscopy (AFM), Park NX-10 model (Park Systems, South Korea), in tapping mode. The scans were performed using a monocrystalline silicon probe, conical-shaped, with a 10° opening angle and 6 nm apex radius. The cantilever was made of the same material, with elastic constant and resonance frequency of 5.1 N m^{-1} and 150 kHz, respectively. The scans were carried out with a relative humidity of 45% at $23 \pm 2^\circ\text{C}$. Films ($\sim 1.0 \text{ cm}^2$ in size) were fixed in the sample holder using double-sided adhesive tape, and four randomly chosen areas ($2.5 \mu\text{m}^2$) of each film were evaluated. Tapping mode was programmed with an amplitude of 30.39 nm, a setpoint of 21.05 nm, and a two-second scan for every 256 pixels line. This process provided a 256×256 data matrix, where each pixel represents a height value.

After generating the topographic images, the height matrices, root mean square (RMS) roughness (Sq), average roughness (Sa), kurtosis (Sk), and skewness (Ssk) were calculated were using WSxM software [57]. A detailed description of these parameters can be found in the literature [6,7,13,55,58].

2.7. Power spectrum density (PSD)

PSD was determined through the Fourier transform of the autocorrelation function of heights distribution, which decomposes surfaces into contributions of different spatial frequencies (represented by wave vectors q). WSxM software was used to calculate one-dimensional PSD (PSD^{1D}) for each line of the scanned image according to Eq. (17).

$$\text{PSD}^{1D}(q_x) = L_x^{-1} \left[\int_{L_x}^h (x, y) e^{-iq_x x} \right]^2 \quad (17)$$

where $h(x, y)$ is the height distribution function, L_x is the number of pixels per line and q_x is the wave vector related to x [13,55].

After PSD^{1D} determination, WSxM software also estimates the surface average PSD, provided as a PSD versus q plot. Following Matos et al. [13], Hurst exponent (H) values were calculated from the average PSD curves using the relation $H = (\alpha - 2)^{-1}$ [55,56], where α is the absolute value of the log [PSD] versus log [q] curve slope.

2.8. Statistical analysis

All results were expressed as mean \pm standard deviation. Significant differences between the mean values were assessed by analyzing variance (one-way ANOVA) followed by the Tukey test. Pearson correlation tests were used to validate the scripts developed by authors. Analyzes were realized in the Statistica software, version 7 (StatSoft, Oklahoma, USA), considering 5% as the level of significance ($p < 0.05$).

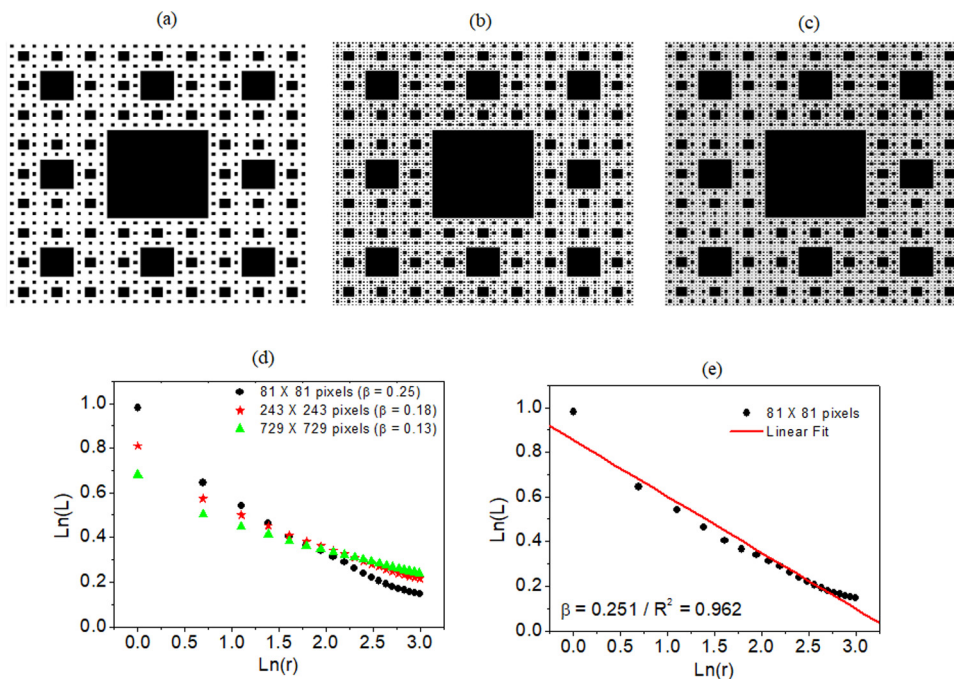


Fig. 2. Numerical simulation of Sierpinski's carpet and its respective lacunar analysis: (a) 81×81 pixels fractal; (b) 243×243 pixels fractal; (c) 729×729 pixels fractal; (d) curves of lacunarity; and (e) linear adjustment of the 81×81 pixels curve. White and black regions in the fractal images correspond to pixels values 1 and 0, respectively.

3. Results and discussion

3.1. Validation of methodology proposed to calculate fractal lacunarity and moran index

Simulated Sierpinski Carpets [Fig. 2(a)–(c)] indicated that the increase of pixels' number slowed down lacunarity decay as a function of the box size [Fig. 2(d)]. The linear regression allowed the calculation of β , as exemplified for 81×81 pixels-image in Fig. 2(e). When the number of pixels was successively increased from 81×81 to 243×243 and 729×729 , lacunarity exponent decreased from 0.25 to 0.18 and 0.13, respectively. Pendleton et al. [59] also found that lacunar analysis using the gliding-box algorithm is strongly affected by image resolution.

The proposed method was also used to analyze self-affine simulated-surfaces with different Hurst exponents [Fig. 3(a)–(e)], where color scale indicates roughness evolution. The height values from simulated images were used to generate the Moran's correlograms [Fig. 4(a)] and curves of separability [Fig. 4(b)], fractal dimension [Fig. 4(c)–(d)], and lacunarity [Fig. 4(e)–(f)]. All fractal dimension and lacunarity curves presented suitable linear adjustment, as exemplified for $H = 0.10$ in Figs. 4(d) and 4(f).

Tables 2 and 3 present a summary of the calculated parameters with their respective standard deviations and the one-way analysis of variance for each of them. ANOVA results showed that W_0 , W_1 , Z e $\eta_{\text{máx}}$ mean values for surfaces with different Hurst exponents did not present significant differences between them. Thus, these parameters were not considered for correlation tests with the lacunarity exponent (β). The correlation graphs between β and the other parameters are shown in Fig. 5.

Fig. 5 shows that μ_0 , μ_1 , D_f , and β decrease with the Hurst exponent increase, while Moran Index presents the opposite behavior. Pearson's correlation coefficient indicated that the lacunarity exponent has a strong positive correlation with μ_0 ($R = 0.8299$, $p = 0.0001$), μ_1 ($R = 0.8224$, $p = 0.0002$) and D_f ($R = 0.9388$, $p = 0.0000002$). On the other hand, β presented a strong negative correlation with the Moran Index ($R = -0.9024$, $p = 0.000004$). Once the lacunarity is a measure of heterogeneity, all presented correlations agreed with the simulated profile smoothing.

H values provide essential information about the correlation and persistence of processes [60], which means that by increasing the surface's H value, the higher and lower heights tend to be followed by higher and lower ones, respectively. This clustering process is accompanied by the appearance of furrows and mountains (Fig. 3). According to Peters [60] and Breslin and Belward [61], the fractal dimension must approach its maximum value when the Hurst exponent decreases [Fig. 5(d)]. Therefore, the roughness profile becomes denser and shows higher spatial frequencies.

The increase of I with the H growth [Fig. 5(c)] showed that spatial autocorrelation analysis was consistent with the theory [26,60]. Moran index as a function of lags dropped more slowly for surfaces with greater Hurst exponents, as

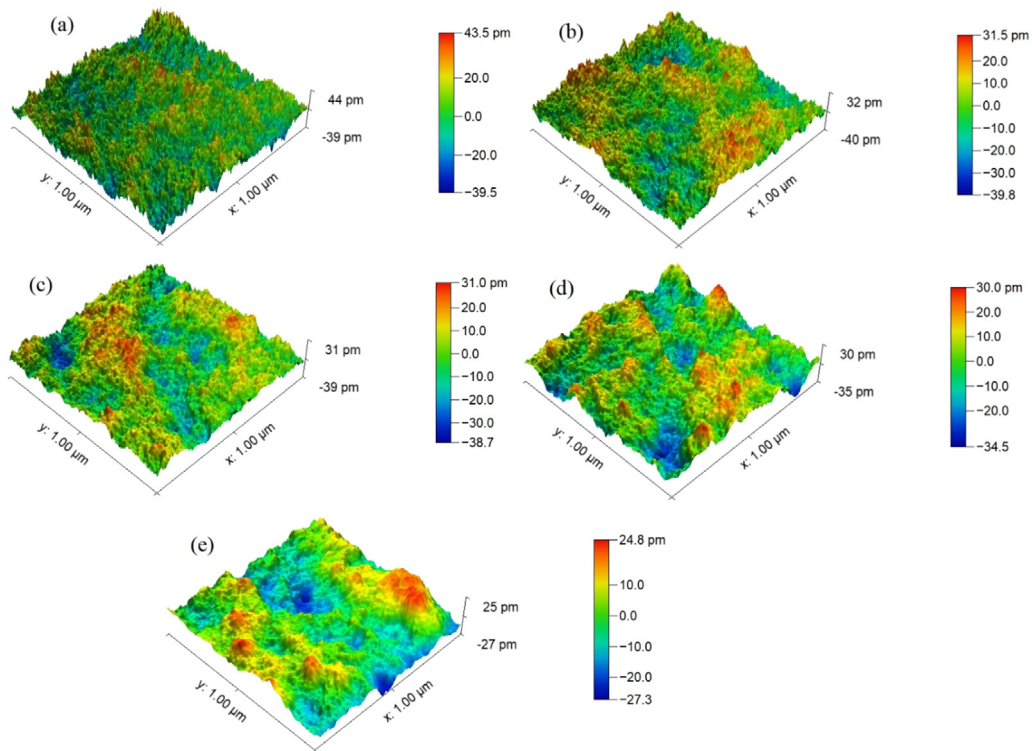


Fig. 3. 3D simulated surfaces with different Hurst exponents: (a) $H = 0.10$; (b) $H = 0.30$; (c) $H = 0.50$; (d) $H = 0.70$; (e) $H = 0.90$.

Table 2

Moran Index (I) for first neighborhood, fractal dimension (D_f), percent of pixels corresponding to valleys (W_0) and peaks (W_1), valleys' average height (μ_0), peaks' average height (μ_1), mean effective height ($Z = \mu_1 - \mu_0$), maximum separability (η_{\max}), and lacunarity exponent (β) of the 3D simulated surfaces.

Parameters	Self-affine artificial surfaces				
	$H = 0.10$	$H = 0.30$	$H = 0.50$	$H = 0.70$	$H = 0.90$
I	0.807 ± 0.017^a	0.924 ± 0.013^b	0.969 ± 0.001^c	0.985 ± 0.004^c	0.993 ± 0.002^c
D_f	2.492 ± 0.014^a	2.407 ± 0.014^b	2.340 ± 0.007^c	2.285 ± 0.022^d	2.222 ± 0.020^e
W_0 (%)	49.9 ± 2.5^a	48.1 ± 2.4^a	49.2 ± 3.9^a	50.2 ± 2.2^a	49.8 ± 1.9^a
W_1 (%)	50.1 ± 2.5^a	51.9 ± 2.4^a	50.8 ± 3.9^a	49.8 ± 2.2^a	50.2 ± 1.9^a
μ_0 (pm)	31.9 ± 0.5^a	31.1 ± 0.8^a	$27.0 \pm 2.7^{a,b}$	23.7 ± 2.7^b	22.3 ± 1.9^b
μ_1 (pm)	47.7 ± 0.6^a	47.0 ± 0.8^a	$42.7 \pm 2.9^{a,b}$	39.3 ± 3.2^b	37.7 ± 2.7^b
Z (pm)	15.8 ± 0.08^a	15.9 ± 0.1^a	15.7 ± 0.2^a	15.6 ± 0.5^a	15.4 ± 0.7^a
η_{\max}	0.639 ± 0.002^a	0.652 ± 0.004^a	0.633 ± 0.003^a	0.641 ± 0.009^a	0.648 ± 0.014^a
β	0.144 ± 0.006^a	$0.120 \pm 0.013^{a,b}$	$0.102 \pm 0.007^{b,c}$	$0.092 \pm 0.010^{b,c}$	0.076 ± 0.014^c

Means followed by the same case letter in the same line do not differ from each other by Tukey test at 5% significance level.

Table 3

Analysis of variance for the new parameters of the simulated self-affine rough surfaces.

Source	DF	I	D_f	W_0	W_1	μ_0	μ_1	Z	η_{\max}	β
Mean square	4	0.01767	0.03312	2.08	2.08	0.000	0.000	0.000	0.000	0.002048
Error	10	0.000	0.000	7.15	7.15	0.000	0.000	0.000	0.000	0.000
Total	14	-	-	-	-	-	-	-	-	-
F -value	-	178.7	126.2	0.292	0.292	14.030	11.306	0.78	2.76	18.604
p -value	-	0.000	0.000	0.877 [¥]	0.877 [¥]	0.000	0.000	0.563 [¥]	0.087 [¥]	0.000

[¥]No significance according to ANOVA at 5% significant level. DF: degree of freedom; I : Moran Index for the first neighborhood; D_f : fractal dimension; W_0 : percent of pixels corresponding to valleys; W_1 : percent of pixels corresponding to peaks; μ_0 : valleys' average height; μ_1 : peaks' average height; Z : mean effective height; η_{\max} : maximum separability; β : lacunarity exponent.

shown in Fig. 4(a). This behavior was already expected once H is a long-range correlation measure, whereas Moran Index is a short-range one [26,60].

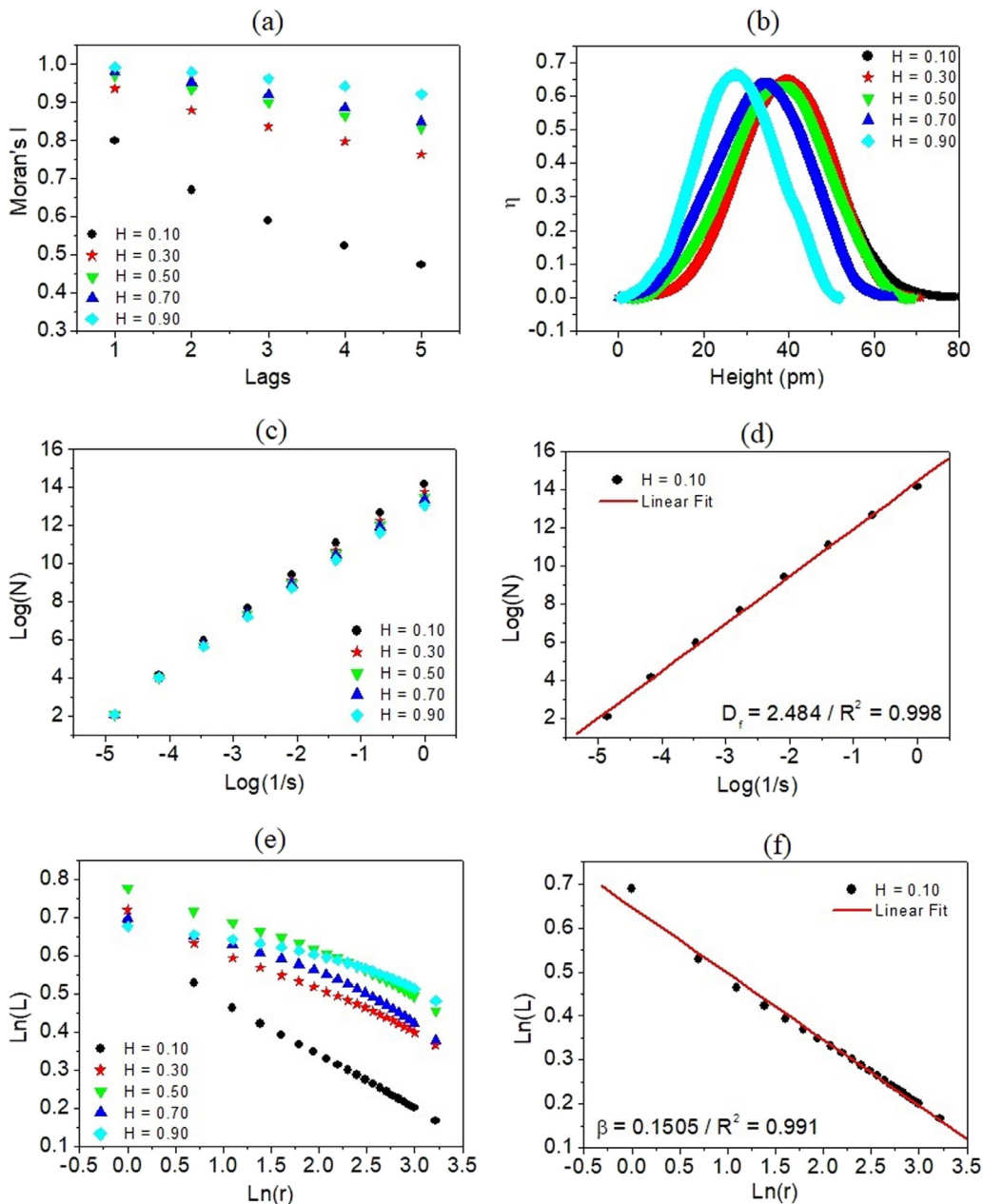


Fig. 4. Surface parameters of the 3D simulated images with different Hurst exponents: (a) Moran correlograms; (b) Otsu separability as a function of ordered heights, from the lowest value (below mean plane) up to the highest one (above mean plane); (c) fractal dimension curves; (d) linear adjustment of fractal dimension curve for $H = 0.10$; (e) lacunarity analysis; and (f) linear adjustment of lacunarity curve with $H = 0.10$.

The maximum separability showed that artificial surfaces have a binary trend once η_{\max} values were greater than 0.5, as shown in Fig. 4(b) and Table 2. The evaluation of the heights histogram's bimodality is important to verify the reliability of lacunarity measurements. Although W_0 , W_1 , μ_0 , μ_1 , and Z are not statistical descriptors of patterns, they are important height parameters due to their similarity with standardized measures described by ISO 25178-2: 2012 [62]. In Figs. 5(a) and 5(b), for example, it is possible to notice that μ_0 and μ_1 decreased with the increase of H , which can be an effect of the profile smoothing.

The combination of the Otsu method and the gliding-box algorithm was consistent with the theory [22] since all lacunarity measurements followed a power law of type $L(p,r) = \alpha r^{-\beta}$ and the linear adjustments for analyzed surfaces [Eq. (15)] showed $R^2 > 0.9$ (see Appendix B). The script developed for lacunarity calculation showed an anomaly behavior in the interval $26 \leq r \leq 249$. In this interval, the exact count of boxes with p lacunar pixels became flawed due to the

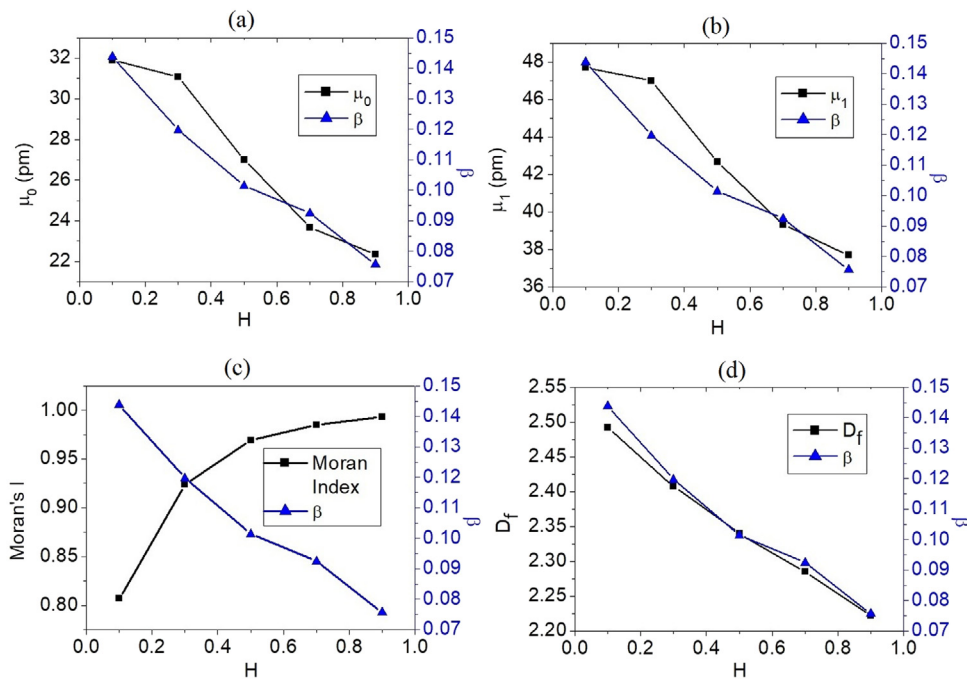


Fig. 5. Study of the correlations between the statistical quality parameters applied to artificial surfaces: (a) β with μ_0 as a function of H, (b) β with μ_1 as a function of H, (c) β with I (1st neighborhood) as a function of H and (d) β with D_f as a function of H.

Table 4

RMS roughness (Sq), mean roughness (Sa), skewness coefficient (Ssk), and kurtosis (Sku) of the AFM images from chitosan films containing 0%, 3%, and 25% of glycerol.

Sample	Sq (nm)	Sa (nm)	Ssk	Sku
#1	3.96 ± 1.12^a	2.91 ± 0.81^a	0.61 ± 0.18^a	6.62 ± 1.48^a
#2	2.38 ± 0.51^a	1.74 ± 0.30^a	-0.51 ± 0.48^b	7.49 ± 3.46^a
#3	12.55 ± 3.29^b	9.33 ± 2.19^b	0.36 ± 0.30^a	5.36 ± 1.42^a

Means followed by the same case letter in the same column do not differ from each other by Tukey test at 5% significance level.

random removal of occupation possibilities that occurred each time the value of r is increased. Such unfeasibility was only overcome for $r > 249$ when the number of possibilities becomes small enough to allow the exact count of boxes. For large values of r , $\ln(L)$ approaches to zero fastly, distorting the curve $\ln(L)$ versus $\ln(r)$ and the slope of the linear adjustment. Therefore, the slope must be calculated considering the curve's first points outside the anomaly region.

Another lacunar analysis critical aspect is the lacunarity exponent possible values. The $\ln(L)$ versus $\ln(r)$ curve's slope [Eq. (15)] can only assume values between 0° and 90° ; thus, the lacunarity exponent varies in the range $0 < \beta < \infty$. If $\beta = 0$, the lacunar distribution is exactly the same in all parts of the image. In contrast, if $\beta \rightarrow \infty$ then $L \rightarrow 0$ according to the power-law $L = \alpha r^{-\beta}$, which means that no lacuna is present on the surface [see Eq. (14)].

The range of $\ln(L)$ values can indicate the surface's lacunar degree, as observed comparing the curves in Figs. 4(e) and 2(d). A surface with large lacunas, a porous sample, must present a more extensive range of $\ln(L)$ values.

3.2. Application to AFM images of chitosan films

Fig. 6 shows the produced chitosan films and their respective AFM images. The difference in the films' texture is only noticeable at the nanoscale. The topographic pattern changed significantly only for the film containing large glycerol concentrations.

Tables 4 and 5 present the height parameters for samples #1, #2, and #3, determined using the commercial software, and the one-way analysis of variance for each of them.

Sq is the standard deviation of surface heights, whereas Sa is the arithmetic mean of the absolute values of the difference between recorded height and average surface height [58]. Sq and Sa are strongly correlated, but Sq presents greater physical significance once it can influence surface energy and surface light scattering [58]. Thus, Sq and Sa values and Tukey test revealed that sample #3 is significantly rougher than those with lower glycerol concentrations. The

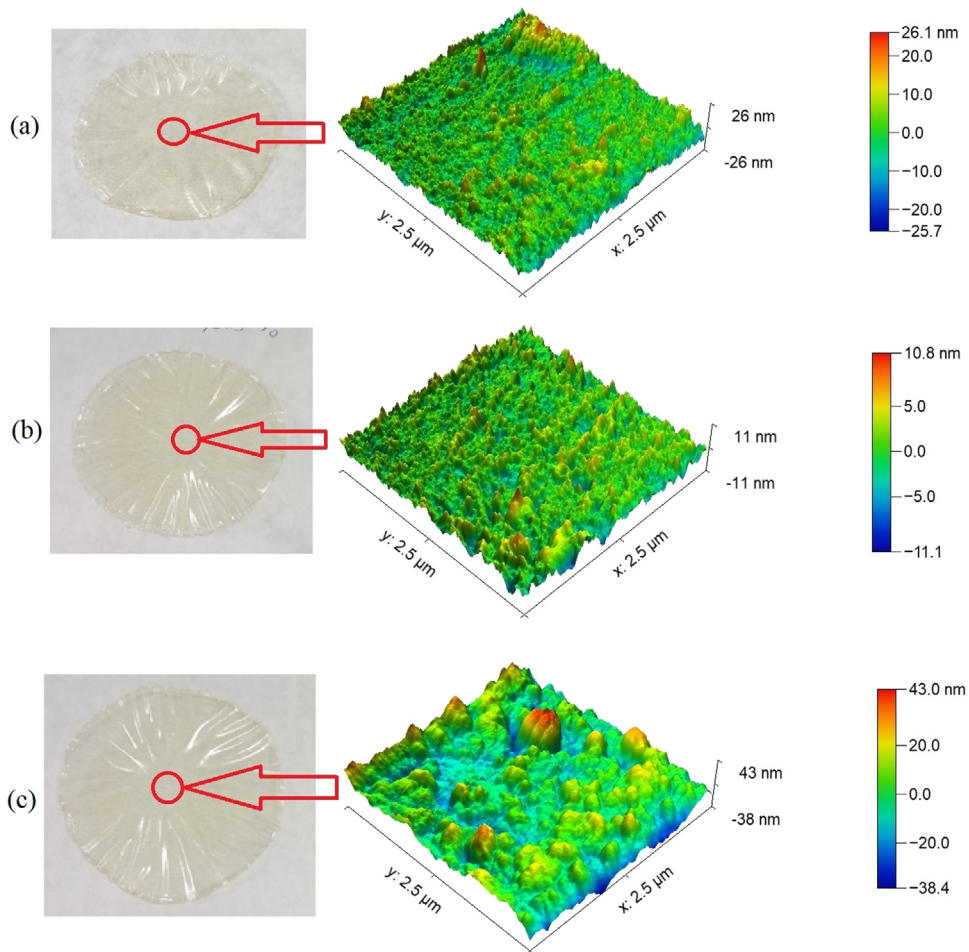


Fig. 6. AFM images of the chitosan films produced by casting: (a) #1 (0% of glycerol); (b) #2 (3% of glycerol); and (c) #3 (25% of glycerol).

Table 5

Analysis of variance of the height parameters from AFM images.

Source	DF	Sq	Sa	Ssk	Sku
Mean square	2	119.7891	66.8004	1.379946	4.5882
Error	9	4.1056	1.8442	0.119350	5.3987
Total	11	–	–	–	–
F-value	–	29.1767	36.2221	11.56217	0.84987
p-value	–	0.000	0.000	0.003261	0.459106 [‡]

[‡]No significance according to ANOVA at 5% significant level. DF: degree of freedom; Sq: RMS roughness; Sa: mean roughness; Ssk: skewness coefficient; Sku: kurtosis.

skewness (Ssk) is the ratio between the average of the third power of height values and the cube of Sq and represents the symmetry degree of the surface heights to the mean plane. It can assume positive and negative values or zero for a symmetrical surface [6,13,58]. A negative Ssk indicates an asymmetrical histogram with a predominance of height values below the mean plane, whereas a positive Ssk indicates the opposite behavior. On the other hand, Sku is the ratio between the average of the fourth power of height values and the fourth power of Sq and describes the shape of heights' probability distribution. Blateyron [58] affirms that spiky surfaces have high kurtosis values. Such surfaces present a predominance of profound valleys and very high peaks. A surface with a Gaussian height distribution, for example, has a kurtosis value equal to 3 [6,58]. Sample #2 presented a predominance of deep valleys (negative Ssk), which suggests pores' presence. Sku values did not show a significant difference among samples.

The parameters presented in Table 4 may not be enough to characterize the films' surface since they undergo great fluctuations due to scale changes and vary significantly for different regions of the same sample. They are very affected by the presence of isolated peaks and valleys [6,13,58]. Gadelmawla et al. [63] point out that real surfaces' geometry is so

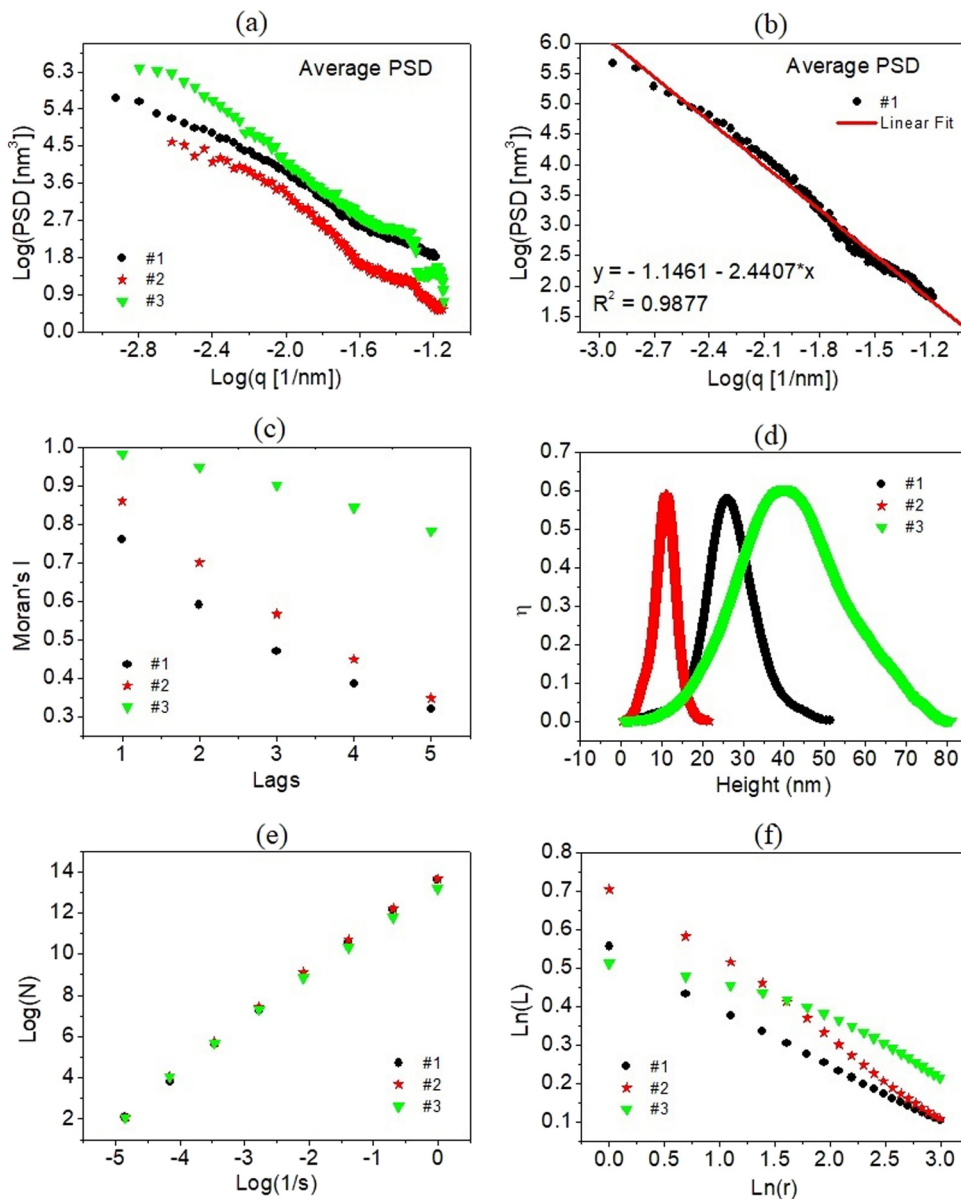


Fig. 7. Surface parameters of the AFM images from chitosan films: (a) average PSD; (b) linear adjustment of PSD curve for sample #1; (c) Moran correlograms; (d) Otsu separability as a function of ordered heights, from the lowest value (below mean plane) up to the highest one (above mean plane); (e) fractal dimension curves; and (f) lacunarity analysis. Samples #1, #2, and #3 correspond to films containing 0%, 3% and 25% of glycerol, respectively.

complex that a limited number of parameters do not allow thorough description. Therefore, a more accurate description can be obtained by introducing novel characterization parameters.

One of the concerns of materials miniaturization is whether their characteristics are preserved or not at smaller scales. Spatial and fractal autocorrelation measures can be valuable tools to assess patterns of thin films at different scales. In this context, we evaluated the average PSD curves, Moran correlograms, Otsu separability, fractal dimension, and lacunarity of the studied chitosan films (Fig. 7). These curves were used to estimate chitosan films' surface parameters (Table 6). Results of the one-way analysis of variance for each parameter are presented in Table 7. All PSD curves and their respective replicates exhibited suitable linear adjustment, as shown in Fig. 7(b) for sample #1 (see Appendix B).

Hurst exponent values (H) increased with the glycerol concentration causing significant changes in the film's roughness [Fig. 7(a) and Table 6]. A Hurst exponent between 0 and 0.5 is characteristic of an inhomogeneous distribution, a spatial frequency series with continuous and alternating high and low-heights. For Hurst exponent equal to 0.5, the distribution of height values is purely random. On the other hand, a Hurst exponent within the range 0.5–1 describes a homogeneous

Table 6

Hurst exponent (H), Moran index (I) for the first neighborhood, fractal dimension (D_f), percent of pixels corresponding to valleys (W_0) and peaks (W_1), valleys' average height (μ_0), peaks' average height (μ_1), mean effective height ($Z = \mu_1 - \mu_0$), maximum separability (η_{\max}), and lacunarity exponent (β) of the chitosan film containing 0% (#1), 3% (#2), and 25% (#3) of glycerol.

Parameters	Chitosan films		
	#1	#2	#3
H	0.18 ± 0.07^a	0.53 ± 0.02^b	0.72 ± 0.06^c
I	0.847 ± 0.070^a	0.877 ± 0.019^a	0.982 ± 0.004^b
D_f	2.39 ± 0.02^a	2.36 ± 0.02^a	2.23 ± 0.04^b
W_0 (%)	51.9 ± 8.3^a	54.5 ± 6.4^a	44.5 ± 6.9^a
W_1 (%)	48.1 ± 8.3^a	45.5 ± 6.4^a	55.5 ± 6.9^a
μ_0 (nm)	19.2 ± 7.3^a	14.9 ± 6.0^a	51.8 ± 26.2^b
μ_1 (nm)	25.2 ± 8.9^a	18.5 ± 6.7^a	70.7 ± 30.0^b
Z (nm)	5.9 ± 1.6^a	3.5 ± 0.6^a	18.9 ± 4.1^b
η_{\max}	0.546 ± 0.033^a	0.545 ± 0.048^a	0.565 ± 0.041^a
β	0.185 ± 0.031^a	0.223 ± 0.037^a	0.120 ± 0.015^b

Means followed by the same case letter in the same line do not differ from each other by Tukey test at 5% significance level.

Table 7

Analysis of variance of the new parameters for the AFM images.

Source	DF	H	I	D_f	W_0	W_1	μ_0	μ_1	Z	η_{\max}	β
Mean square	2	0.29945	0.02016	0.02911	105.43	105.43	1621.128	3229.92	274.803	0.000	0.011
Error	9	0.00301	0.00174	0.000	52.38	52.38	257.593	340.37	6.649	0.0017	0.000
Total	11	–	–	–	–	–	–	–	–	–	–
F -value	–	99.316	11.575	34.21	2.0127	2.0127	6.29337	9.4893	41.331	0.280	12.716
p -value	–	0.000	0.00325	0.000	0.189 [‡]	0.189 [‡]	0.0195	0.0061	0.000	0.762 [‡]	0.002

[‡]No significance according to ANOVA at 5% significant level. DF: degree of freedom; H : Hurst exponent; I : Moran Index for the first neighborhood; D_f : fractal dimension; W_0 : percent of pixels corresponding to valleys; W_1 : percent of pixels corresponding to peaks; μ_0 : valleys' average height; μ_1 : peaks' average height; Z : mean effective height; η_{\max} : maximum separability; β : lacunarity exponent.

distribution, a spatial frequency series presenting height-values with repetition probability greater than 50%, which indicates a tendency and is called a persistent process [55,60]. Such differences can be observed comparing Figs. 6(b) and 6(c).

Although samples #1 and #2 have statistically different mean H (Table 6), their Moran correlograms are very similar [Fig. 7(c)], which can be confirmed by I values and the comparison between Figs. 6(a) and 6(b). It is important to emphasize that only a few points were considered for estimating the average PSD [64], while the entire height matrix was used to construct the correlograms. Thus, Moran's correlogram provides an interesting and complementary characterization of the spatial roughness distribution.

Fractal dimension (D_f) values (Table 6) were determined based on the curves in Fig. 7(e). D_f reduced from film #1 to #3, confirming the topographic profile smoothing at large glycerol concentrations. Particle clusters characterized this surface smoothing, possibly formed due to polarity differences between glycerol and chitosan molecules [38,65]. Clusters contribute to a greater spacing between the valleys, forming channels that favor liquids flow. Pinto et al. [38] showed that an increase of glycerol concentration in chitosan films enhanced its hydrophilic character, both because of the glycerol polarity and the surface morphology changes.

Changes in the separability curves' profile [Fig. 7(d)] and η_{\max} value (Table 6) suggested variations in the film's thickness. Comparing the mean thickness of samples #1 (0.14 ± 0.02 mm), #2 (0.19 ± 0.04 mm), and #3 (0.31 ± 0.04 mm), only the last one differ significantly. Therefore, a more detailed investigation of the relationship between separability curve and film thickness is essential.

The percentage of valley's (W_0) and peak's (W_1) pixels did not change significantly among samples. However, film #2 presented a higher kurtosis value ($Sku = 7.49$), negative skewness ($Ssk = -0.51$), and 54.5% of valley pixels, suggesting a more porous aspect. Among the films' lacunarity exponents, sample #2 presented a higher β value (0.223). The valleys' average height (μ_0), peaks' average height (μ_1), and average effective height (Z) for film #3 differed statistically among samples, confirming the thickness increase. For higher glycerol concentrations, the number of plasticizer molecules between the chitosan chains increases [65], enlarging the intermolecular distance and weakening its bonds.

Regarding the estimates of lacunarity exponents (β), the Otsu method presented maximum separability (η_{\max}) greater than 0.5 for all samples [Table 6 and Fig. 7(d)], confirming the images' binary trend. Furthermore, all linear adjustments for the lacunarity curves exhibited $R^2 > 0.9$ (see Appendix B). The curves in Fig. 7(f) and the β mean values (Table 6) also showed that only film #3 indicated a significantly lower lacunar change rate.

Our results also suggested that chitosan films containing 25% of glycerol have a more homogeneous and less complex topography, with a predominance of low spatial frequencies. AFM images already pointed out topographic differences

among films (Fig. 6), but this behavior agrees with the correlogram in Fig. 7(c), where sample # 3 showed a strong spatial correlation between height values. Notwithstanding, proposed scripts proved to be promising tools to complement the topographic analysis of AFM images.

4. Conclusions

This work presents a methodology to improve AFM images' characterization by using fractal lacunarity and Moran Index, which was successfully applied to analyze chitosan films. Our results also showed that:

- (i) Identifying surface lacunas using Otsu method introduced new parameters (W_0 , W_1 , μ_0 , μ_1 , and η_{\max}) to topographical analysis, giving greater statistical significance lacunarity measurements.
- (ii) The gliding-box algorithm, adapted to the R programming language, provided greater control and accuracy over the lacunarity exponent estimation.
- (iii) Lacunarity analysis is affected by images' pixels number. Thus, comparisons between different samples are limited to images with identical resolution.
- (iv) Determination of Moran index allowed access to new topographical information of surfaces, showing potential as a complementary measure for the Hurst exponent.
- (v) Application of the methodology using AFM images of chitosan films suggested that the proposed surface parameters could be a complementary tool to the quality processing control of thin films.

CRediT authorship contribution statement

Erveton P. Pinto: Writing - original draft, Methodology, Investigation, Data curation, Software, Validation, Formal analysis, Writing - editing. **Marcelo A. Pires:** Methodology, Validation, Review. **Robert S. Matos:** Data curation, Review. **Robert R.M. Zamora:** Review, Supervision, Resources. **Rodrigo P. Menezes:** Review, Supervision, Resources. **Raquel S. Araújo:** Review, Supervision. **Tiago M. de Souza:** Review, Supervision.

Declaration of competing interest

The authors declare that they have no known competing financial interests or personal relationships that could have appeared to influence the work reported in this paper.

Data availability

The raw/processed data required to reproduce these findings cannot be shared at this time as the data also forms part of an ongoing study.

Acknowledgments

We would like to thank Fundação de Amparo à Pesquisa do Estado do Amapá (FAPEAP) and CNPq for the support (EDITAL PRONEM, grant # 95/2018).

Appendix A. Scripts used in this paper

The scripts used in this paper are openly available at:
https://github.com/erveton/Otsu_Binarization_AFM_Image
https://github.com/erveton/Lacunarity_AFM_Image
https://github.com/erveton/Moran_Index_AFM_Image

Appendix B. Supplementary material

Supplementary data to this article can be found online at: <https://github.com/erveton/Supplementary-material.git>.

References

- [1] Y.-R. Jeng, C.-C. Gao, Changes of surface topography during wear for surfaces with different height distributions, *Tribol. Trans.* 43 (2000) 749–757, <https://doi.org/10.1080/10402000008982404>.
- [2] S. Sundararajan, B. Bhushan, Topography-induced contributions to friction forces measured using an atomic force/friction force microscope, *J. Appl. Phys.* 88 (2000) 4825, <https://doi.org/10.1063/1.1310187>.
- [3] D.E. Packham, Surface energy, surface topography and adhesion, *Int. J. Adhes. Adhes.* 23 (2003) 437–448, [https://doi.org/10.1016/S0143-7496\(03\)00068-X](https://doi.org/10.1016/S0143-7496(03)00068-X).
- [4] P.S.P. Herrmann, M.A.P. da Silva, R. Bernardes, A.E. Job, L.A. Colnago, J.E. Frommer, L.H.C. Mattoso, Microscopia de Varredura por Força: uma Ferramenta Poderosa no Estudo de Polímeros, *Polim.: Cienc. Tecnol.* 7 (1997) 51–61, <https://doi.org/10.1590/S0104-14281997000400009>.
- [5] G. Binnig, C.F. Quate, C. Gerber, Atomic force microscope, *Phys. Rev. Lett.* 56 (1986) 930–933, <https://doi.org/10.1103/PhysRevLett.56.930>.
- [6] S. Stach, W. Sapota, Ş. Tălu, A. Ahmadpourian, C. Luna, N. Ghobadi, A. Arman, M. Ganji, 3-D surface stereometry studies of sputtered TiN thin films obtained at different substrate temperatures, *J. Mater. Sci., Mater. Electron.* 28 (2016) 2113–2122, <https://doi.org/10.1007/s10854-016-5774-9>.
- [7] Ş. Tălu, I.A. Morozov, R.P. Yadav, Multifractal analysis of sputtered indium tin oxide thin film surfaces, *Appl. Surf. Sci.* 484 (2019) 892–898, <https://doi.org/10.1016/j.apsusc.2019.04.170>.
- [8] Ş. Tălu, S. Abdolghaderi, E.P. Pinto, R.S. Matos, M. Salerno, Advanced fractal analysis of nanoscale topography of Ag/DLC composite synthesized by RF-PECVD, *Surf. Eng.* 36 (2020) 713–719, <https://doi.org/10.1080/02670844.2019.1710937>.
- [9] Ş. Tălu, R.S. Matos, E.P. Pinto, S. Rezaee, M. Mardani, Stereometric and fractal analysis of sputtered Ag–Cu thin films, *Surf. Interfaces* 21 (2020) 100650, <https://doi.org/10.1016/j.surfin.2020.100650>.
- [10] F.M. Mwema, O.P. Oladipo, T.S. Sathiaraj, E.T. Akinlabi, Atomic force microscopy analysis of surface topography of pure thin aluminum films, *Mater. Res. Express* 5 (2018) 046416, <https://iopscience.iop.org/article/10.1088/2053-1591/aabe1b>.
- [11] X. Liu, D. Song, X. He, Z. Wang, M. Zeng, K. Deng, Nanopore structure of deep-burial coals explored by AFM, *Fuel* 246 (2019) 9–17, <https://doi.org/10.1016/j.fuel.2019.02.090>.
- [12] R.S. Matos, G.A.C. Lopes, N.S. Ferreira, E.P. Pinto, J.C.T. Carvalho, S.S. Figueiredo, A.F. Oliveira, R.R.M. Zamora, Superficial characterization of Kefir biofilms associated with Açai and Cupuaçu extracts, *Arab. J. Sci. Eng.* 43 (2018) 3371–3379, <https://doi.org/10.1007/s13369-017-3024-y>.
- [13] B.S. Matos, I.S. Pinheiro, R.R. Souza, G.Q. Paes de Castro, E.P. Ramos, R.S. Pinto, R.S. Silva Jr., H.D. da Fonseca Filho, 3D micromorphology evaluation of kefir microbial films loaded with extract of amazon rainforest fruit cupuaçu, *Micron* 142 (2021) 102996, <https://doi.org/10.1016/j.micron.2020.102996>.
- [14] B.B. Mandelbrot, *The Fractal Geometry of Nature*, W.H. Freeman and Company, New York, 1983.
- [15] A. Arman, Ş. Tălu, C. Luna, A. Ahmadpourian, M. Naseri, M. Molamohammadi, Micromorphology characterization of copper thin films by AFM and fractal analysis, *J. Mater. Sci., Mater. Electron.* 26 (2015) 9630–9639, <https://doi.org/10.1007/s10854-015-3628-5>.
- [16] M. Nasehnejad, G. Nabiyouni, M.G. Shahraki, Thin film growth by 3D multi-particle diffusion limited aggregation model: Anomalous roughening and fractal analysis, *Phys. A* 493 (2018) 135–147, <https://doi.org/10.1016/j.physa.2017.09.099>.
- [17] G. Taraschi, J.B. Florindo, Computing fractal descriptors of texture images using sliding boxes: An application to the identification of Brazilian plant species, *Phys. A* 545 (2020) 123651, <https://doi.org/10.1016/j.physa.2019.123651>.
- [18] B.B. Mandelbrot, A fractal's lacunarity, and how it can be tuned and measured, in: T.F. Nonnenmacher, G.A. Losa, E.R. Weibel (Eds.), *Fractals in Biology and Medicine*, Birkhäuser, Basel, Switzerland, 1994, https://doi.org/10.1007/978-3-0348-8501-0_2.
- [19] R.E. Plotnick, R.H. Gardner, W.W. Hargrove, K. Prestegard, M. Perlmutter, Lacunarity analysis: A general technique for the analysis of spatial patterns, *Phys. Rev. E* 53 (1996) 5461–5468, <https://doi.org/10.1103/PhysRevE.53.5461>.
- [20] G. Landini, Fractals in microscopy, *J. Microsc.* 241 (2011) 1–8, <https://doi.org/10.1111/j.1365-2818.2010.03454.x>.
- [21] S.W. Myint, N. Lam, A study of lacunarity-based texture analysis approaches to improve urban image classification, *Environ. Urban Syst.* 29 (2005) 501–523, <https://doi.org/10.1016/j.compenvurbsys.2005.01.007>.
- [22] M.R.B. Dias, D. Dornelas, W.F. Balthazar, J.A.O. Huguenin, L. da Silva, Lacunarity study of speckle patterns produced by rough surfaces, *Phys. A* 486 (2017) 328–336, <https://doi.org/10.1016/j.physa.2017.05.022>.
- [23] D. Risović, H. Gebavi, M. Ivanda, Influence of fractal and lacunar characteristic of a nanostructured substrate on SERS enhancement, *Appl. Surf. Sci.* 537 (2021) 147915, <https://doi.org/10.1016/j.apsusc.2020.147915>.
- [24] A. Pander, T. Onishi, A. Hatta, H. Furuta, Study of self-organized structure in carbon nanotube forest by fractal dimension and lacunarity analysis, *Mater. Charact.* 160 (2020) 110086, <https://doi.org/10.1016/j.matchar.2019.110086>.
- [25] N. Cocu, R. Harrington, M. Hullé, M.D.A. Rounsevell, Spatial autocorrelation as a tool for identifying the geographical patterns of aphid annual abundance, *Agric. For. Entomol.* 7 (2005) 31–43, <https://doi.org/10.1111/j.1461-9555.2005.00245.x>.
- [26] A. Shortridge, Practical limits of Moran's autocorrelation index for raster class maps, *Comput. Environ. Urban Syst.* 31 (2007) 362–371, <https://doi.org/10.1016/j.compenvurbsys.2006.07.001>.
- [27] D.A. Griffith, The moran coefficient for non-normal data, *J. Statist. Plann. Inference* 140 (2010) 2980–2990, <https://doi.org/10.1016/j.jspi.2010.03.045>.
- [28] Y. Chen, New approaches for calculating moran's index of spatial autocorrelation, *PLoS One* 8 (2013) e68336, <https://doi.org/10.1371/journal.pone.0068336>.
- [29] D. Liu, Q. Zhao, S. Guo, P. Liu, L. Xiong, X. Yu, H. Zou, Y. Zeng, Z. Wang, Variability of spatial patterns of autocorrelation and heterogeneity embedded in precipitation, *Hydrol. Res.* 50 (1) (2019) 215–230, <https://doi.org/10.2166/nh.2018.054>.
- [30] N. Diawara, L. Waller, R. King, J. Lorio, Simulations of local Moran's index in a spatio-temporal setting, *Comm. Statist. Simulation Comput.* 48 (2018) 1849–1859, <https://doi.org/10.1080/03610918.2018.1425441>.
- [31] M.R. Shirzadi, M. Javanbakht, N. Jesri, A. Saghafipour, Spatial distribution of cutaneous leishmaniasis cases referred to health centers of three Khorasan provinces in Iran using ge-ographical information system, *Iran. J. Publ. Health.* 48 (2019) 1885–1892, <https://doi.org/10.18520/ijph.v48i10.3497>.
- [32] <https://cran.r-project.org/> (Accessed March 2019).
- [33] E. Vélez-Peña, J. Pérez-Obando, D. Pais-Ospina, D.A. Marín-Silva, A. Pinotti, A. Cánneva, J.A. Donadelli, L. Damonte, L.R. Pizzio, P. Osorio-Vargas, J.A. Rengifo-Herrera, Self-cleaning and antimicrobial photo-induced properties under indoor lighting irradiation of chitosan films containing Melon/TiO₂ composites, *Appl. Surf. Sci.* 508 (2020) 144895, <https://doi.org/10.1016/j.apsusc.2019.144895>.
- [34] J.T. Martins, M.A. Cerqueira, A.A. Vicente, Influence of α -tocopherol on physicochemical properties of chitosan-based films, *Food Hydrocolloids* 27 (2012) 220–227, <https://doi.org/10.1016/j.foodhyd.2011.06.011>.
- [35] M. Sabbah, P. Di Pierro, M. Cammarota, E. Dell'Olmo, A. Arciello, R. Porta, Development and properties of new chitosan-based films plasticized with spermidine and/or glycerol, *Food Hydrocolloids* 87 (2019) 245–252, <https://doi.org/10.1016/j.foodhyd.2018.08.008>.
- [36] M.F. Di Filippo, S. Panzavolta, B. Albertini, F. Bonvicini, G.A. Gentilomi, R. Orlacchio, N. Passerini, A. Bigi, L.S. Dolci, Functional properties of chitosan films modified by snail mucus extract, *Int. J. Biol. Macromol.* 143 (2020) 126–135.

- [37] Y. Zhong, X. Song, Y. Li, Antimicrobial, Physical and mechanical properties of kudzu starch–chitosan composite films as a function of acid solvent types, *Carbohydr. Polymers* 84 (2011) 335–342, <https://doi.org/10.1016/j.carbpol.2010.11.041>.
- [38] E. Pinto, W. Tavares, R. Matos, A. Ferreira, R. Menezes, M. Costa, T. Souza, I. Ferreira, F. Sousa, R. Zamora, Influence of low and high glycerol concentrations on wettability and flexibility of chitosan biofilms, *Quím. Nova* (2018) 1109–1116, <https://doi.org/10.21577/0100-4042.20170287>.
- [39] L. Cai, H. Shi, A. Cao, J. Jia, Characterization of gelatin/chitosan polymer films integrated with docosaheptaenoic acids fabricated by different methods, *Sci. Rep.* 9 (2019) 8375, <https://doi.org/10.1038/s41598-019-44807-x>.
- [40] <http://gwyddion.net/download.php> (Accessed March 2018).
- [41] A.R. Backes, A new approach to estimate lacunarity of texture images, *Pattern Recognit. Lett.* 34 (2013) 1455–1461, <https://doi.org/10.1016/j.patrec.2013.05.008>.
- [42] O. Gereben, Lacunarity analysis of atomic configurations: application to ethanol–water mixtures, *Phys. Rev. E* 92 (2015) 033305, <https://doi.org/10.1103/PhysRevE.92.033305>.
- [43] C. Allain, M. Cloitre, Characterizing the lacunarity of random and deterministic fractal sets, *Phys. Rev. A* 44 (1991) 3552–3558, <https://doi.org/10.1103/PhysRevA.44.3552>.
- [44] N. Otsu, A threshold selection method from gray-level histograms, in: *IEEE Transactions on Systems, Man, and Cybernetics*, Institute of Electrical and Electronics Engineers (IEEE), 1979, pp. 62–66.
- [45] D.H. Xie, M. Lu, Y.F. Xie, D. Liu, X. Li, A fast threshold segmentation method for froth image base on the pixel distribution characteristic, *PLoS One* 14 (2019) e0210411, <https://doi.org/10.1371/journal.pone.0210411>.
- [46] H. Du, X. Chen, J. Xi, An improved background segmentation algorithm for fringe projection profilometry based on Otsu method, *Opt. Commun.* 453 (2019) 124206, <https://doi.org/10.1016/j.optcom.2019.06.044>.
- [47] K. Fukunaga, *Introduction to Statistical Pattern Recognition*, second ed., Academic Press, USA, 2013.
- [48] M.O.C. Salcedo, R.R.M. Zamora, J.C.T. Carvalho, Estudio fractal de la superficie de la hoja de la especie vegetal *Copaifera* sp. haciendo uso del Microscopio de Fuerza Atómica-AFM, *Revista ECIPerú* 13 (2016) 10–16, <https://doi.org/10.33017/RevECIPeru2016.0002/>.
- [49] R. Seffrin, E.C. de Araújo, C.L. Bazzi, Análise espacial de área aplicada a produtividade de soja na região oeste do Paraná utilizando o software R, *Rev. Bras. Geoma.* 6 (2018) 23–43, <https://github.com/r-spatial/spdep/> (Accessed March 2020).
- [50] R.H.C. de Melo, A. Conci, How succolarity could be used as another fractal measure in image analysis, *Telecommun. Syst.* 52 (2011) 1643–1655, <https://doi.org/10.1007/s11235-011-9657-3>.
- [51] http://rosettacode.org/wiki/Rosetta_Code (Accessed March 2020).
- [52] B.N. Persson, O. Albohr, U. Tartaglino, A.I. Volokitin, E. Tosatti, On the nature of surface roughness with application to contact mechanics, sealing, rubber friction and adhesion, *J. Phys.: Condens. Matter* 17 (2004) R1–R62, <https://doi.org/10.1088/0953-8984/17/1/R01>.
- [53] https://github.com/plang85/rough_surfaces (Accessed March 2020).
- [54] T.D.B. Jacobs, T. Junge, L. Pastewka, Quantitative characterization of surface topography using spectral analysis, *Surf. Topogr.: Metrol. Prop.* 5 (2017) 013001, <https://doi.org/10.1088/2051-672X/aa51f8>.
- [55] P.S. Lang, *Multi-Scale Modelling of Thermohydro–Mechanical–Chemical Processes in Fractured Rocks*, Department of Earth Science and Engineering Faculty of Engineering, Imperial College London, 2016, p. 203, <http://www.wsxm.es/download.html> (Accessed March 2018).
- [56] F. Blateyron, The areal field parameters, in: *Characterisation of Areal Surface Texture*, 2013, pp. 15–43, https://doi.org/10.1007/978-3-642-36458-7_2.
- [57] D.E. Pendleton, A. Dathe, P. Baveye, Influence of image resolution and evaluation algorithm on estimates of the lacunarity of porous media, *Phys. Rev. E* 72 (2005) 041306, <https://doi.org/10.1103/PhysRevE.72.041306>.
- [58] E.E. Peters, *Chaos and Order in the Capital Markets: A New View of Cycles, Prices, and Market Volatility*, second ed., John Wiley & Sons, New York, 1996.
- [59] M.C. Breslin, J.A. Belward, Fractal dimensions for rainfall time series, *Math. Comput. Simulation* 48 (1999) 437–446, [https://doi.org/10.1016/S0378-4754\(99\)00023-3](https://doi.org/10.1016/S0378-4754(99)00023-3).
- [60] <http://www.iso.org> (Accessed March 2019).
- [61] E.S. Gadelmawla, M.M. Koura, T.M.A. Maksoud, I.M. Elewa, H.H. Soliman, Roughness parameters, *J. Mater. Process. Technol.* 123 (2002) 133–145, [https://doi.org/10.1016/S0924-0136\(02\)00060-2](https://doi.org/10.1016/S0924-0136(02)00060-2).
- [62] I. Horcas, R. Fernandez, J.M. Gomez-Rodriguez, J. Colchero, J. Gomez-Herrero, A.M. Baro, WSXM: a software for scanning probe microscopy and a tool for nanotechnology, *Rev. Sci. Instrum.* 78 (2007) 013705, <https://doi.org/10.1063/1.2432410>.
- [63] J.N. Israelachvili, *Intermolecular and Surface Forces*, third ed., Academic Press, Elsevier, USA, 2011.